



A Low-wear Planar-contact Silicon Raceway for Microball Bearing Applications

by C. Mike Waits

ARL-TR-4796

April 2009

NOTICES

Disclaimers

The findings in this report are not to be construed as an official Department of the Army position unless so designated by other authorized documents.

Citation of manufacturer's or trade names does not constitute an official endorsement or approval of the use thereof.

Destroy this report when it is no longer needed. Do not return it to the originator.

Army Research Laboratory

Adelphi, MD 20783-1197

ARL-TR-4796

April 2009

A Low-wear Planar-contact Silicon Raceway for Microball Bearing Applications

C. Mike Waits

Sensors and Electron Devices Directorate, ARL

REPORT DOCUMENTATION PAGE				Form Approved OMB No. 0704-0188	
<p>Public reporting burden for this collection of information is estimated to average 1 hour per response, including the time for reviewing instructions, searching existing data sources, gathering and maintaining the data needed, and completing and reviewing the collection information. Send comments regarding this burden estimate or any other aspect of this collection of information, including suggestions for reducing the burden, to Department of Defense, Washington Headquarters Services, Directorate for Information Operations and Reports (0704-0188), 1215 Jefferson Davis Highway, Suite 1204, Arlington, VA 22202-4302. Respondents should be aware that notwithstanding any other provision of law, no person shall be subject to any penalty for failing to comply with a collection of information if it does not display a currently valid OMB control number.</p> <p>PLEASE DO NOT RETURN YOUR FORM TO THE ABOVE ADDRESS.</p>					
1. REPORT DATE (DD-MM-YYYY) April 2009		2. REPORT TYPE Final		3. DATES COVERED (From - To) January to July 2008	
4. TITLE AND SUBTITLE A Low-wear Planar-contact Silicon Raceway for Microball Bearing Applications				5a. CONTRACT NUMBER	
				5b. GRANT NUMBER	
				5c. PROGRAM ELEMENT NUMBER	
6. AUTHOR(S) C. Mike Waits				5d. PROJECT NUMBER H94 94MDP0	
				5e. TASK NUMBER	
				5f. WORK UNIT NUMBER	
7. PERFORMING ORGANIZATION NAME(S) AND ADDRESS(ES) U.S. Army Research Laboratory ATTN: AMSRD-ARL-SE-DP 2800 Powder Mill Road Adelphi, MD 20783-1197				8. PERFORMING ORGANIZATION REPORT NUMBER ARL-TR-4796	
9. SPONSORING/MONITORING AGENCY NAME(S) AND ADDRESS(ES)				10. SPONSOR/MONITOR'S ACRONYM(S)	
				11. SPONSOR/MONITOR'S REPORT NUMBER(S)	
12. DISTRIBUTION/AVAILABILITY STATEMENT Approved for public release; distribution unlimited.					
13. SUPPLEMENTARY NOTES					
14. ABSTRACT <p>As silicon rotary micro-electromechanical systems (MEMS) devices become critical components to power generation and sensor platforms, it is crucial to develop bearing mechanisms that can achieve speed and reliability requirements without increasing cost and complexity. Microball bearings have proven simple to fabricate and capable of achieving high speeds. However, previous microball raceway implementations showed substantial degradation in performance and required cleaning steps to improve reliability. Furthermore, large surface roughness on the raceway thrust surface caused increased wear and friction. In this work, the silicon raceway is modified by shifting the rotor bond interface, minimizing both wear and debris generation within the bearing. We developed a modified fabrication process that eliminates the source of the raceway thrust surface roughness. These modifications led to continuous and repeatable operation for over 4,500,000 revolutions with no degradation in performance. Our testing demonstrated speeds in excess of 85,000 rpm, more than twice that of previous designs.</p>					
15. SUBJECT TERMS Microball bearing, microturbine, microfabrication					
16. SECURITY CLASSIFICATION OF:			17. LIMITATION OF ABSTRACT UU	18. NUMBER OF PAGES 34	19a. NAME OF RESPONSIBLE PERSON C. Mike Waits
a. REPORT Unclassified	b. ABSTRACT Unclassified	c. THIS PAGE Unclassified			19b. TELEPHONE NUMBER (Include area code) (301) 394-0057

Contents

List of Figures	iv
List of Tables	v
1. Background	1
2. Design	2
2.1 Modified Bearing Design	2
2.2 Platform and Bearing Design	7
3. Device Fabrication	10
3.1 Rotor Fabrication.....	10
3.2 Turbine Manifold Fabrication	12
4. Experimental Setup	12
5. Results and Discussion	15
5.1 Experimental Results.....	15
5.2 Raceway Inspection.....	17
6. Conclusions	20
7. References	21
List of Symbols, Abbreviations, and Acronyms	24
Distribution List	25

List of Figures

Figure 1. Key fabrication steps for the microball bearing.	3
Figure 2. Schematic drawing of the planar-contact bearing V.2 implemented in the spiral-groove turbopump.	4
Figure 3. An SEM image that shows the worn bond interface of the planar-contact raceway after <100,000 revolutions.	4
Figure 4. (a) Original planar bearing fabrication process using nested photoresist and silicon dioxide masks and (b) new planar bearing fabrication process eliminating the nested masking technique for a smooth bearing surface.	6
Figure 5. SEM image showing the fabrication defects at the corner of the raceway journal.	7
Figure 6. Illustrations showing: (a) cross-sectional view of the radial in-flow turbine supported by the encapsulated microball bearing, (b) radial in-flow air turbine design, and (c) planar-contact bearing orientation.	8
Figure 7. Schematic of the planar-contact design employing an off-center journal.	9
Figure 8. Key fabrication process steps for the microturbine platform.	10
Figure 9. Optical photograph of a silicon trench cross section demonstrating the buildup of photoresist at the corners of a trench. Note the different photoresist thickness between the wafer surface and the trench bottom.	11
Figure 10. Optical image showing the turbine side of a released rotor.	12
Figure 11. Illustration of the packaged turbopump without the pump plumbing layer to characterize the turbine operation.	13
Figure 12. Illustration of the mechanical jig with the turbopump inside.	14
Figure 13. Schematic of the experimental apparatus used for testing the microturbine tribology device.	15
Figure 14. Turbine characterization up to 10,000 rpm in air before and after packaging the pump manifold layer.	16
Figure 15. Turbine characterization curve with pump manifold before 50,000 revolutions and after exceeding 2,000,000 revolutions.	16
Figure 16. Demonstration of high-speed operation with the planar-contact V.2 bearing and the radial in-flow air turbine.	17
Figure 17. SEM image showing the top down view of the bearing thrust surface using the modified spray coat process.	18
Figure 18. SEM images of the rotor raceway thrust and radial surface for (a) Device 1 and (b) Device 2.	18
Figure 19. SEM image showing a close-up of the radial raceway surfaces for the new design with the bond interface moved away from the ball wear track.	19

List of Tables

Table 1. Parameters for the planar-contact bearing.	9
--	---

INTENTIONALLY LEFT BLANK.

1. Background

Since the mid 1990s, micro-electromechanical systems (MEMS) technologies have received increased attention for use in portable (<10 W) power applications, therefore, referred to as “Power MEMS.” Due to the significant energy density and power density contained within the fuel (at only 10% efficiency, diesel fuel can yield 4.2 MJ/kg, which is 10 times more than 0.36 MJ/kg for primary batteries), liquid hydrocarbon fuels are favorable energy sources as compared to conventional battery chemistries. Power MEMS devices that have been investigated for portable power and take advantage of the high density energy stored in hydrocarbons are typically rotational-based devices that can include gas turbine generators (1–3), steam engine generators (4), rotary engine generators (5), and balance of plant components for fuel cells (6, 7).

These rotary Power MEMS devices require microfabricated silicon rotary elements for micro-motors, micro-generators, and micro-turbomachinery. Within these devices the friction and wear characteristics of the bearing mechanism are the primary determinant to device performance, reliability, and lifetime. Understanding the tribology characteristics and developing bearing designs to minimize both friction and wear is critical to developing a robust bearing mechanism for use in MEMS technologies.

Both contact and non-contact bearings have been investigated for rotary motion; however, no known successful commercial implementations exist. MEMS bearing research has been plagued by short lifetimes with poor reliability and robustness. Non-contact bearing designs include magnetic, electrostatic, or hydrostatic air bearings (8–13). These bearings have high-speed capabilities (>1 Mrpm in the case of air bearings) and can be controlled during operation but only at the cost of large external pressurization, complex fabrication requirements, and complex electronic control and integration schemes. Contact bearing designs are limited to center-pin bushings that are simple to fabricate and operate but impart a large amount of friction due to sliding contact. The large friction ultimately limits the operation to low speeds (14–17).

Microball bearings are an emerging technology for rotational-based micro devices that offer simple fabrication and passive operation when compared to non-contact bearings. Microball bearings also offer low friction operation of dynamic rolling friction when compared to sliding-based contact bearings. Initial microball bearing research was focused on measuring the coefficient of friction between stainless steel microballs and silicon grooves (18–20). Both linear and rotary micromotors for sensor platforms were developed that used microballs placed within small silicon grooves to support a slider or rotor, respectively (21, 22). In both cases the slider or rotor is forced to contact the microballs only by gravity or electrostatic means (i.e., the rotor is not fully constrained), and therefore, was severely limited in applications.

An encapsulated bearing mechanism was developed to fully constrain the rotor without the need for external forces (23–25). In previous work, the microball bearing tribology mechanisms were studied and an empirical relationship between the bearing friction torque and the normal load/speed was developed (25). Two key issues were found during that work: (1) there was significant surface roughness on the raceway thrust surface caused by the fabrication process and (2) large debris generation was caused by the bond interface at the radial contact surface. The debris generation caused a drastic drop in performance, and therefore, required periodic cleaning to bring the device back to original performance.

In this work, I modified the design and fabrication of planar-contact bearings to eliminate debris generation and reduce friction, enabling a high-speed and high reliability bearing mechanism. I used an air turbine platform to characterize the modified bearings and inspected the raceway to verify low wear operation over long operating periods.

2. Design

2.1 Modified Bearing Design

The design of the microball bearing raceway is limited to the silicon microfabrication techniques (23). I chose square-groove annular trenches for good dimensional control, repeatability, and uniformity across the raceway diameter and because they are readily achieved using deep reactive ion etching (DRIE) techniques. Figure 1 illustrates the three primary fabrication steps to realize a rotor supported by the microball bearings. The bearing raceway is fabricated from two silicon layers with annular square-grooves etched into the surface (figure 1, Step 1) that are bonded together (figure 1, Step 2) to form an encapsulated microball bearing. Subsequently, the outer surfaces of the bonded stack are then etched to release the rotor so that it is only supported via the microball bearing (figure 1, Step 3).

The operation of the bearing mechanism is performed by integrating a motor or turbine on one side of the rotor. Since the journal is offset to ensure the microball rides on a planar thrust surface, a net-positive force on the rotor in the proper direction is required to ensure proper contact on the correct surface.

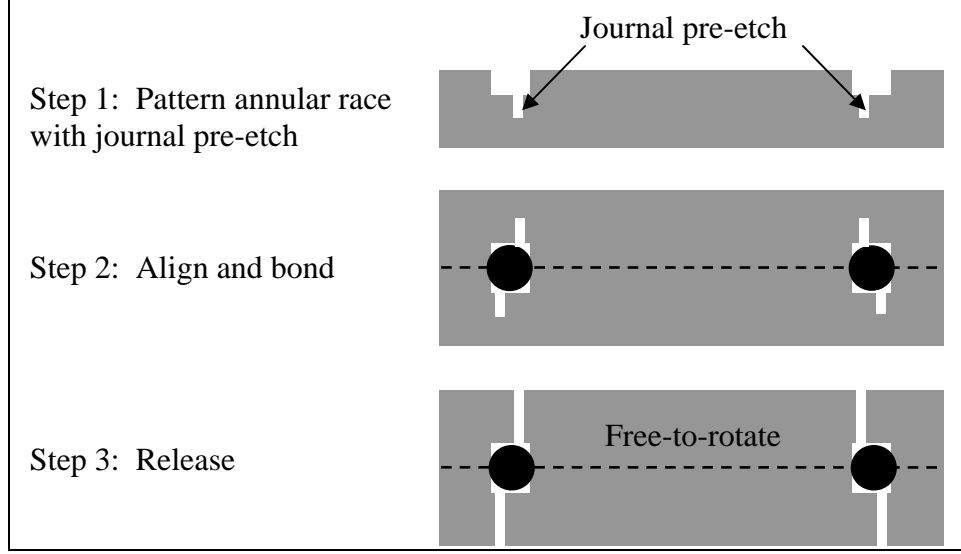


Figure 1. Key fabrication steps for the microball bearing.

The bond interface between the two rotor layers and the journal etch used to release the rotor are critical features within the raceway. In previous work, the design of these features limited both the performance of the bearing and the ability to maintain a constant performance for an extended number of revolutions. Here, the design of the raceway in Step 1 is modified to increase the performance as well as the ability to maintain the performance for a high number of revolutions. Steps 2 and 3 in the fabrication of the microball bearing remain the same from previous work (23).

The previous planar-contact raceway design is shown in figure 2a. In this design, the annular square-groove raceway etched into each silicon die with the same depth creates a bond interface at the center of the raceway and within the track of the microball bearing. Debris is generated within the raceway when the compressive stress exerted on the raceway is larger than the fracture strength of silicon. The maximum compressive stress exerted on the raceway is determined by the following equation (26):

$$\sigma_{\max} = \frac{3Q}{2\pi ab}, \quad (1)$$

where Q denotes the load exerted normal to the race from the ball, a is the semi-major axis radius of an elliptical contact area, and b is the semi-minor axis radius for an elliptical contact. On the thrust surface, the maximum compressive stress is calculated to be <1.6 GPa (for a contact area of $>2 \mu\text{m}^2$ and load of 500 mN), well below the typical fracture strength of silicon, which is between 7 and 30 GPa. The maximum compressive stress exerted on a corner similar to the bond interface ranges from >30 GPa (1 μm radius of curvature, $<0.4 \mu\text{m}^2$ contact area) to 7 GPa (23 μm radius of curvature, $1.5 \mu\text{m}^2$ contact area).

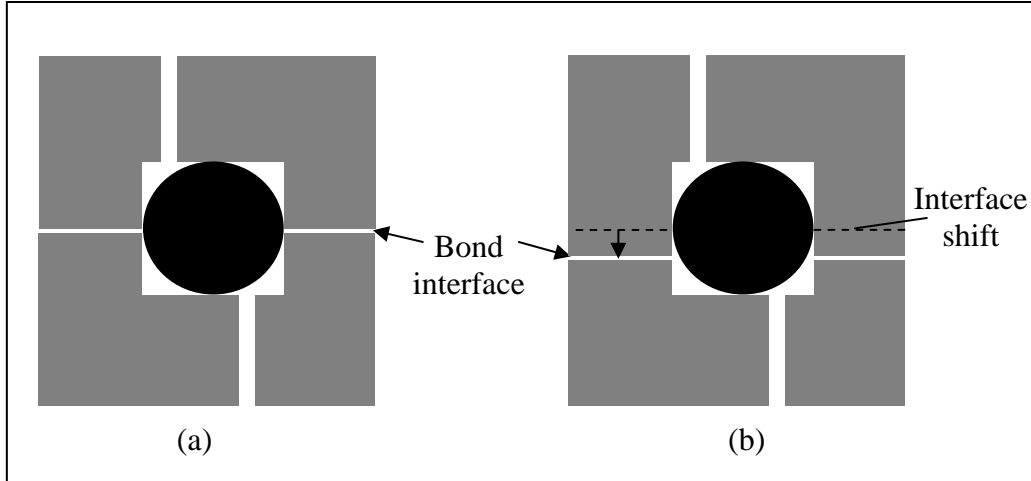


Figure 2. Schematic drawing of the planar-contact bearing V.2 implemented in the spiral-groove turbopump.

The large amount of compressive stress at the bond interface corners leads to subsurface fracturing and debris generation. This is confirmed by inspection of the raceway from previous experiments. Figure 3 shows a scanning electron microscope (SEM) image of an extremely worn bond interface after less than 100,000 revolutions. The microball wear track wore away 10 μm of silicon at the center of a 50- μm wear track and caused a significant amount of debris. Multiple cleaning steps after operation were required to maintain the performance of the microball bearing designed with the bond interface at the center of the raceway. In this work, the bond interface is moved out of the microball wear track (figure 2b) to eliminate the high compressive stress at the corners, thereby reducing the potential debris generation and wear. The maximum compressive stress on the radial raceway surface is then the same as the thrust surface, which exhibits less than a 1- μm -deep wear track.

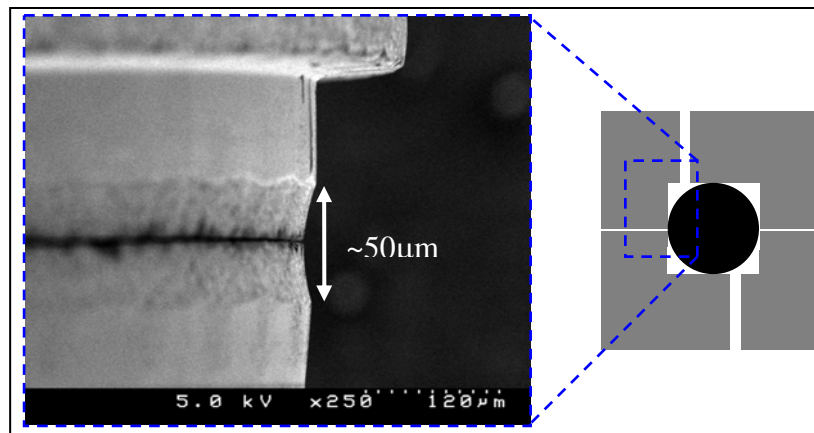


Figure 3. An SEM image that shows the worn bond interface of the planar-contact raceway after <100,000 revolutions.

The second critical feature of the raceway design is the journal at the base of the square-groove trench. Figure 4a shows the fabrication flow used in previous work to develop the planar-contact bearing. In that work, the raceway was fabricated using a nested masking process where the journal was first patterned and etched using photoresist (Step 2 to Step 3) and then the annular square-groove was etched using an underlying silicon dioxide layer (Step 4 to Step 5). In this manner, the corner of the journal etch is “pushed” down during the etch step. The top surface, where the microball bearing rides, was inspected using SEM analysis. A roughening of the surface was observed (figure 5) and was believed to arise from the dynamics of the passivation-etch cycles occurring at the journal corner. The silicon at the base of the square-groove trench etches faster than the fluorocarbon passivation layer on the journal sidewall causing pillars of passivation material to develop during the etch step. Once the aspect ratio of the pillars becomes too large, the pillars fall over and mask the edge of the corner on the square-groove trench.

To eliminate the artifact observed at the journal corner using the nested-masking process, I developed a modified spray coat process (figure 4b). In this process, the annular square-groove trench is first patterned and etched using a photoresist or hard masking material (Step 1 to Step 2). Then, photoresist is patterned at the base of the square-groove trench using a photoresist spray coater and contact lithography (Step 3). The journal is then etched using the photoresist to protect the raceway surface (Step 4) and, finally, the photoresist layer is removed (Step 5).

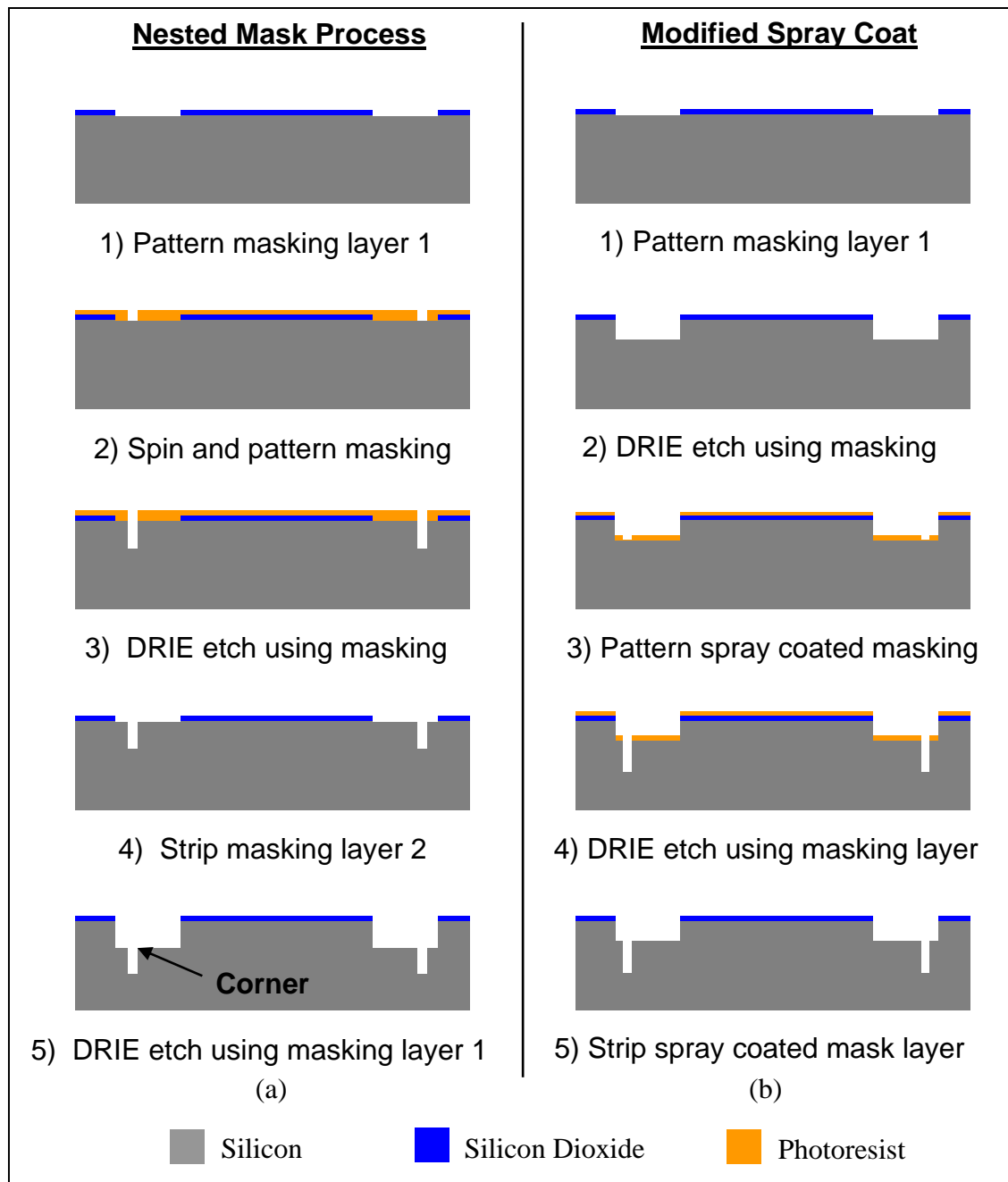


Figure 4. (a) Original planar bearing fabrication process using nested photoresist and silicon dioxide masks and (b) new planar bearing fabrication process eliminating the nested masking technique for a smooth bearing surface.

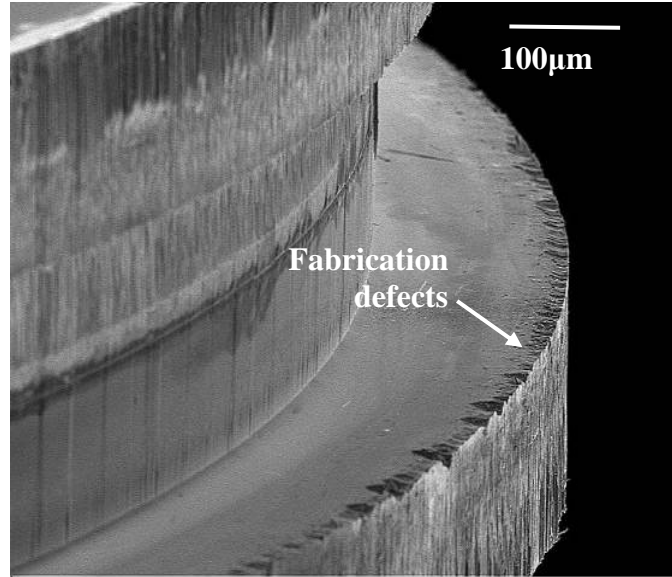


Figure 5. SEM image showing the fabrication defects at the corner of the raceway journal.

2.2 Platform and Bearing Design

A radial in-flow air turbine platform is used for controlled actuation of the rotor supported by the microball bearings at the periphery (figure 6a). In this work, I designed the platform to characterize the newly developed planar-contact raceway design for maximum speed and reliability. The air turbine device is composed of the rotor layer (10 mm diameter rotor) that houses the microball raceway and a turbine manifold layer that contains the turbine inlet and outlet orifices and provides a capping of the fluidic pathways of the device. Turbine operation is achieved by providing pressurized air through 24 inlet orifices aligned just outside of the stator vanes. These vanes turn the flow through the rotor blades and out the exit of the turbine (figure 6b). Patterned tracking marks at the center of the turbine rotor allow the rotational speed to be monitored during operation. More details on the design of the turbine platform have been reported elsewhere (25).

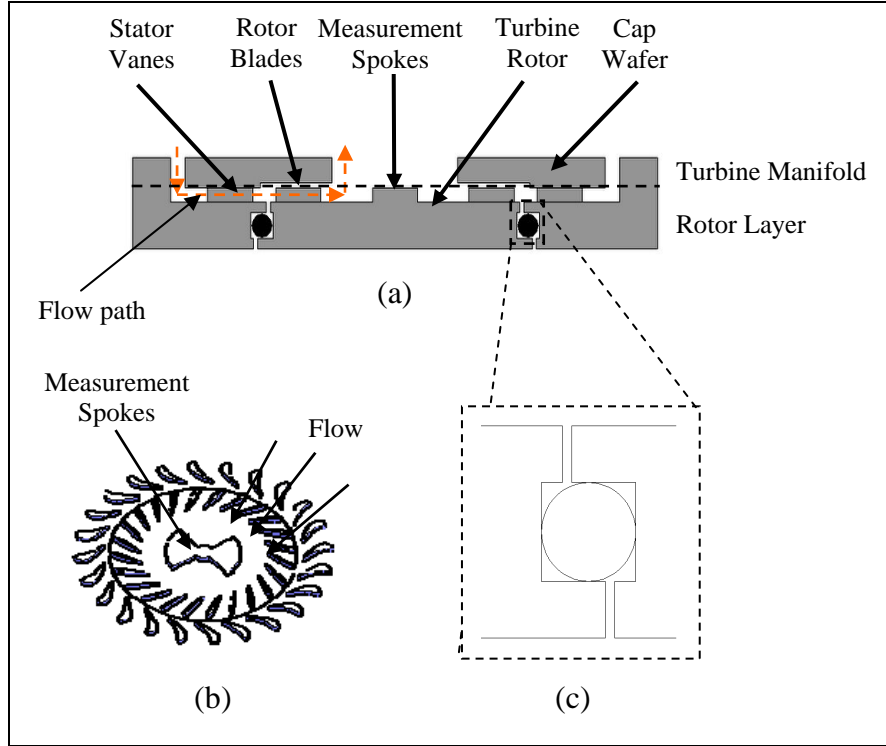


Figure 6. Illustrations showing: (a) cross-sectional view of the radial in-flow turbine supported by the encapsulated microball bearing, (b) radial in-flow air turbine design, and (c) planar-contact bearing orientation.

The microball bearing is placed at the periphery of the turbine rotor to provide high stability (figure 6c). The design of the raceway is shown in figure 7 and the dimensions are provided in table 1. From figure 7, $h_1 + h_2$ and w_1 must be large enough to ensure proper encapsulation of a 285 μm diameter microball, w_2 must be made large enough to provide sufficient clearance for rotation, and w_3 must be made large enough to extend past the entire contact area between the microball and silicon race. Given predicted fabrication tolerances, the choice of w_3 in table 1 ensures that the race extended well past the expected contact area. On the other hand, the remaining length, $w_1 - (w_2 + w_3)$, must be sufficient enough to still capture the rotor when, during fabrication and assembly, the load is flipped in the opposite direction.

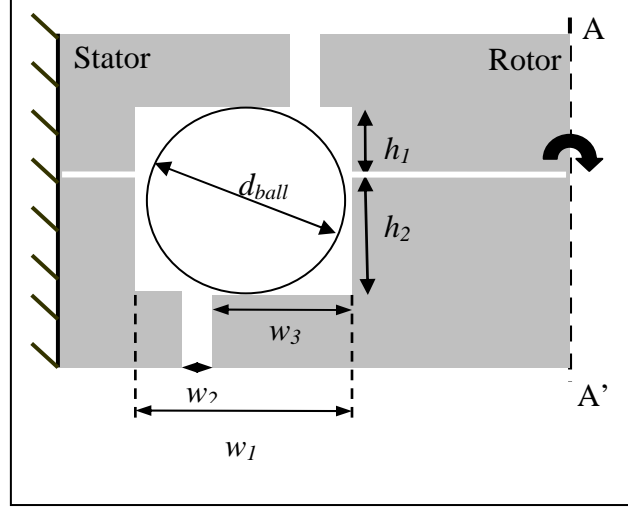


Figure 7. Schematic of the planar-contact design employing an off-center journal.

Table 1. Parameters for the planar-contact bearing.

Bearing Race Parameter	Designed Dimension (μm)
d_{ball}	285
$h + \delta h$	290
$w_1 + \delta w_1$	290
$w_2 + \delta w_2$	30
w_3	190

The bond interface was moved away from the wear track, which was observed to be 50 μm wide (figure 3). Therefore, the bond interface was moved 50 μm from the center of the raceway by etching the raceway 95 μm (h_1) on the turbine side and 195 μm (h_2) on the opposite side (figure 7). The journal design is kept 30 μm (w_2) wide and 70 μm (w_3) from the closest edge to ensure the journal edge is not in the path of the microball, while at the same time not allowing for a large sag in the improper direction.

The planar-contact design is limited to operation in only one load direction, i.e., the direction from A' to A along the rotational axis (figure 7). If the bearing were to operate in the opposite orientation, the ball would revert back to riding on a corner with a higher wear rate (23). The pressure across the flat rotor surface must be kept above the pressure across the turbine side to maintain proper normal force direction. During testing this is achieved by sealing the flat surface of the rotor, which allows pressure to build up that is equal to the turbine inlet pressure.

3. Device Fabrication

The turbine platform is composed of two separate layers: the rotor layer and turbine manifold. Each layer is fabricated separately and then aligned and clamped together by the device fixture to seal the fluidic paths (figure 8).

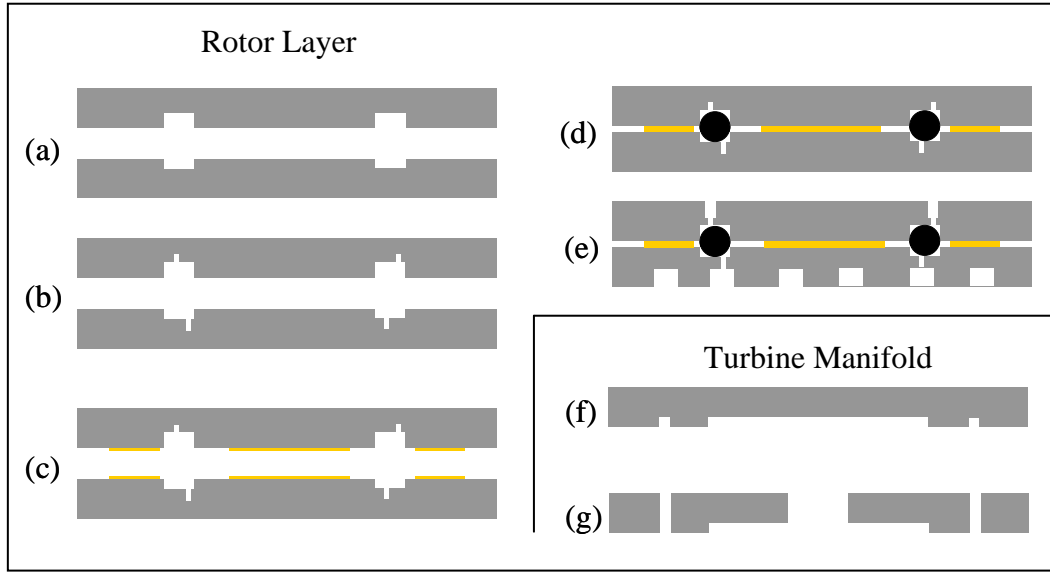


Figure 8. Key fabrication process steps for the microturbine platform.

3.1 Rotor Fabrication

The rotor layer fabrication starts with two double-sided polished, 4-in silicon wafers. The annular raceway is defined in each of the layers. On the bottom rotor layer, the raceway is etched shallow to 95 μm , while the opposing wafer is etched to 195 μm (figure 8a). The different raceway etch depths allow the bond interface between the two layers to be 50 μm from the center of the raceway. This way the microball will not contact the interface. After the raceway is etched, journals are patterned using spray coated photoresist and etched using DRIE (figure 8b).

Using a contact profilometer, I found the thickness of the spray-coated photoresist to be much thinner at the bottom of the trench than on the wafer surface (figure 9). In addition, the two raceway depths had two different photoresist thicknesses. Although the same photoresist spray coating recipe was applied to both, the 95 μm deep raceway had a photoresist layer approximately 8 μm , while the 195 μm deep raceway had a photoresist layer approximately 3.6 μm . I measured the thickness of the spray coated photoresist on the top surface to be 10 μm . Each race should have specific exposure and development times associated with the different layer thickness at the bottom of the raceway. An exposure time of 10 s and a development time

of 90 s were sufficient to clear away the 8 μm thick photoresist. The 3.6 μm thick photoresist became overexposed and developed (30 μm wide line became 35 μm wide). To ensure complete development, the patterns on the wafer surface were exposed for an additional 5 s using a second optical mask.

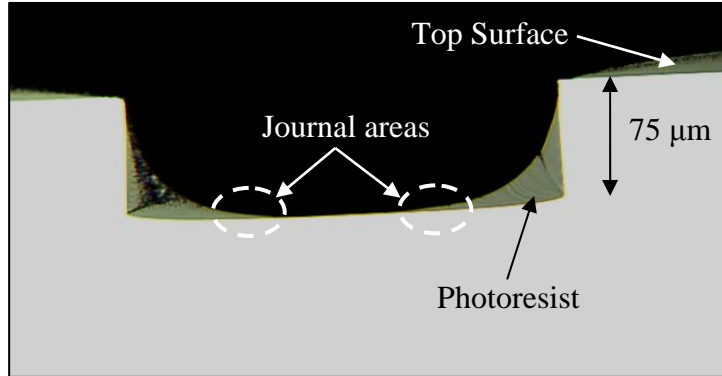


Figure 9. Optical photograph of a silicon trench cross section demonstrating the buildup of photoresist at the corners of a trench. Note the different photoresist thickness between the wafer surface and the trench bottom.

Once the journals are completed, the next steps are to bond the two rotor layers together. First, the surfaces are cleaned using an O_2 plasma ash and second a metal adhesion layer is deposited on both wafer surfaces to be bonded using electron beam deposition (figure 8c). The adhesion layer is composed of a chromium (Cr) (50 nm), gold (Au) (50 nm), gold-tin (AuSn) (1 μm), and Au (50 nm) stack for eutectic bonding. The metal layers are patterned using a shadow mask made from a silicon wafer during the deposition. The wafers are diced after metal deposition and microballs are placed within the silicon raceways in a full compliment fashion, totaling up to 110 microballs. The two layers are aligned using microballs in etched pits with a depth of 145 μm (similar to our previous work [9]). This enables alignments within 5 μm and even better alignments possible with smaller etched pit tolerances. The eutectic bond is performed with a temperature of 330 $^\circ\text{C}$ and an H_2N_2 forming gas to help breakup any oxidation and remove organic material from the surfaces (figure 8d).

The final step in the fabrication of the rotor layer is to release the rotor using the patterned turbine and journal on each side of the die (figure 8e). These layers are patterned into silicon dioxide prior to dicing the wafers. The topside of the rotor is released using a 45 μm wide annular ring, which is 15 μm wider than the journal to ensure the complete width of the journal is released. The etch depth required to meet the pre-etched journal and release the rotor from the topside is 145 μm .

The radial in-flow air turbine is patterned into the silicon dioxide layer on the turbine side of the rotor. The torque provided by the turbine to the first order using Euler turbomachinery equation is directly proportional to the blade height. To increase the torque provided by the turbine a

large blade height is needed; however, the uniformity of the etch process worsens with etch depth. A non-uniform release results in etched pits between the microballs, which could protrude into the microball contact path and hamper the performance of the bearing (9). A height of 200 μm was chosen to provide enough torque and to obtain a uniform release with measured uniformities less than 1 μm across the rotor diameter. Figure 10 shows a completed turbine rotor.

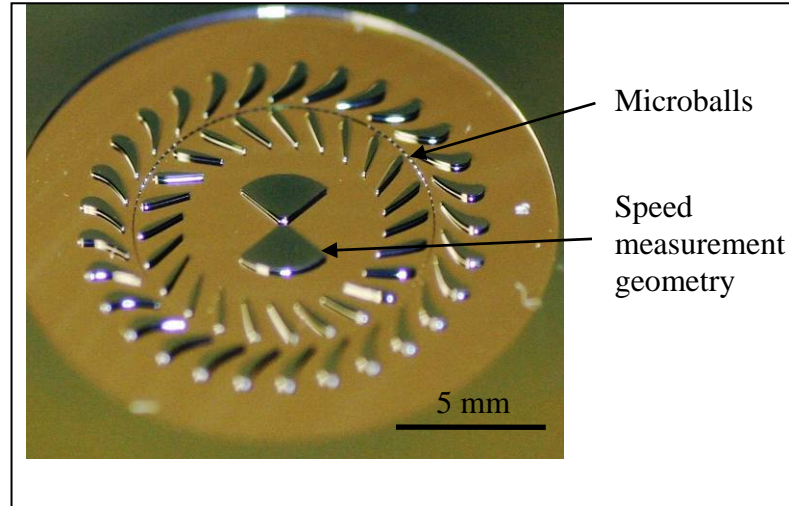


Figure 10. Optical image showing the turbine side of a released rotor.

3.2 Turbine Manifold Fabrication

The turbine manifold is fabricated using two DRIE etching steps. The first step (figure 8f) patterns a cavity to provide sufficient clearance for the turbine blades. The normal force on the turbine rotor causes the rotor to sag into the cavity during operation. The depth of the cavity is chosen such that the clearance above the turbine blades is less than 20% of the 200- μm blade height. This is sufficient to allow most of the flow to produce torque on the rotor. The second DRIE step completes the through etches from the backside for the turbine exhaust and fluidic ports (figure 8g).

4. Experimental Setup

Two packaging schemes, Scheme 1 and Scheme 2, were used to investigate the bearing performance. Scheme 1 was used to investigate the high-speed capabilities of the raceway. Scheme 2 was developed to test a micropump using the bearing mechanism (27). The micropump device was also used to investigate the reliability.

The packaging scheme for Scheme 1 is shown in figure 11. The fixture seals on the topside of the device using a gasket and thus creates a thrust pressure plenum pressurized by the turbine

driving fluid. The pressurized backside causes the direction of the normal force to be towards the turbine exhaust (downward in figure 11). The package is manufactured using conventional alumina machining techniques and is composed of a lid and a base plate with fluidic ports. The turbine device is placed on top of o-rings to separate the turbine inlet from the turbine exit. The thrust pressure plenum is created by placing o-rings between the topside of the device and a gasket. The o-ring seals are compressed using screws that attach the lid to the base plate. Access to the speed measurement geometry on the turbine rotor is provided within the fixture for an optical displacement probe.

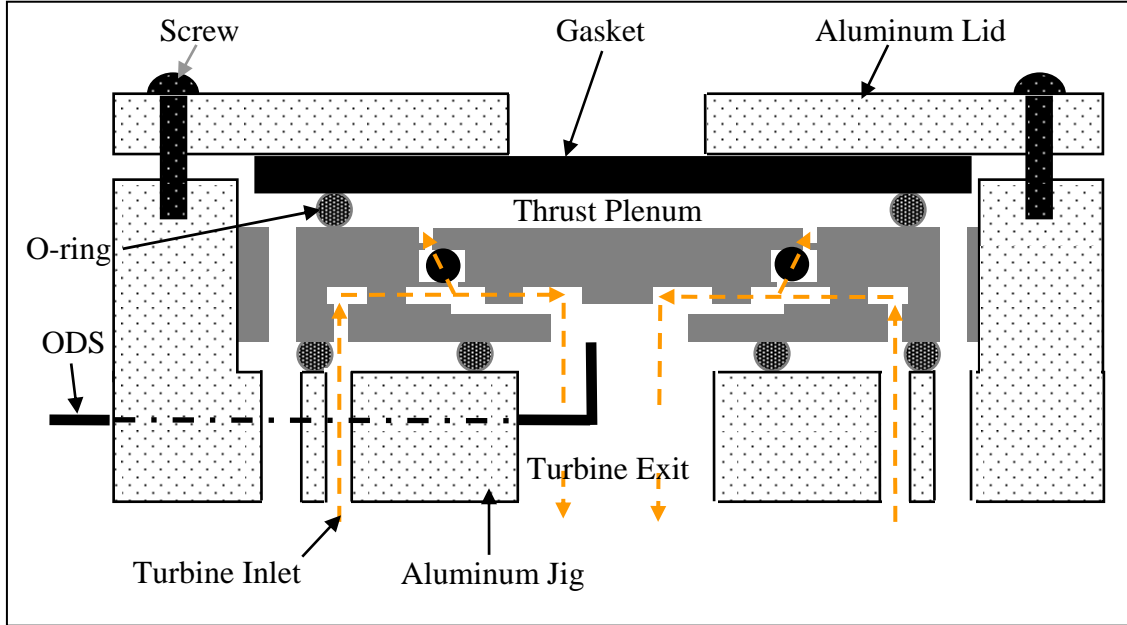


Figure 11. Illustration of the packaged turbopump without the pump plumbing layer to characterize the turbine operation.

The packaging scheme used in Scheme 2 uses the same fixture; however, instead of a gasket/o-ring to seal the topside of the device, a pump manifold provides the sealing mechanism (figure 12). A key difference between the packaging schemes is the amount of air drag. In Scheme 1, air drag is negligible since the o-ring thickness of 1.6 mm creates a large cavity. In Scheme 2, the gap between the topside rotor surface and the pump manifold is 15 μm , which increases the effect of air drag by more than 100 times.

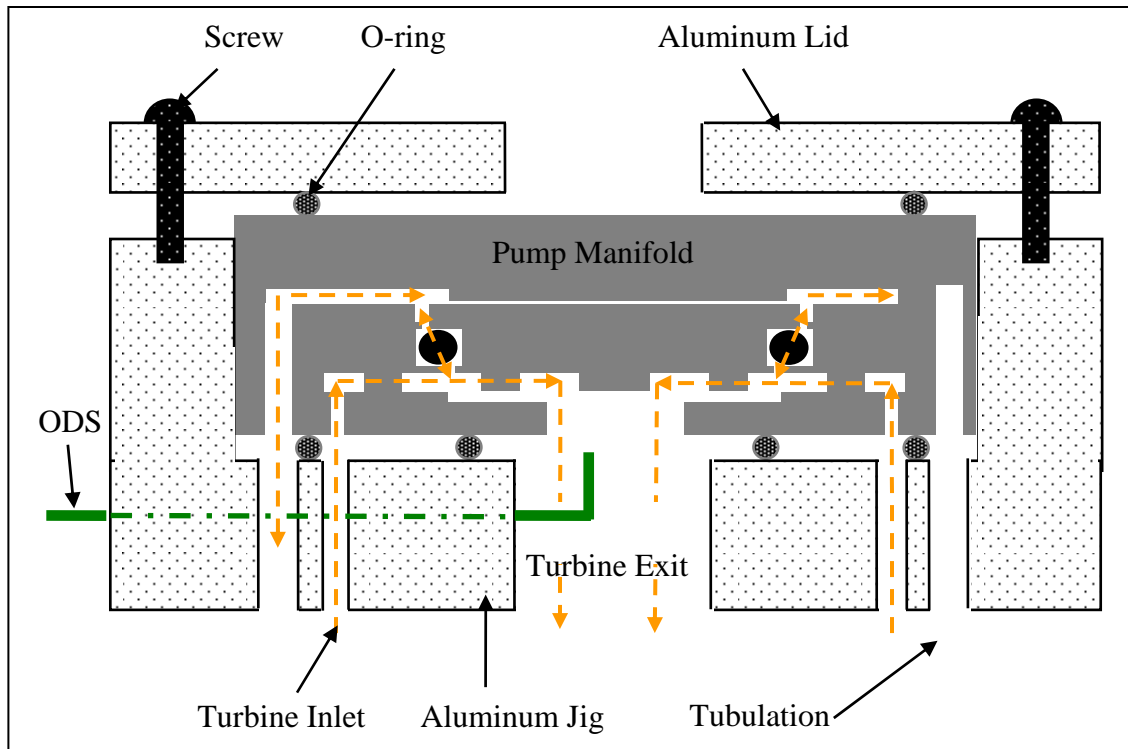


Figure 12. Illustration of the mechanical jig with the turbopump inside.

The gas control and measurement setup and the speed measurement setup with a computer interface are shown in figure 13. The turbine inlet flow comes from a house nitrogen line that is controlled using a manual in-line valve. The flow rate and pressure are measured just prior to entering the device. To measure the rotational speed of the rotor, an optical displacement sensor is placed below the speed measurement marks at the center of the rotor. The raw voltage contains continuous pulses corresponding to a passing by mark. The signal is read into LabView and the rotational speed is deduced from the frequency found using a Fast Fourier Transform (FFT) algorithm.

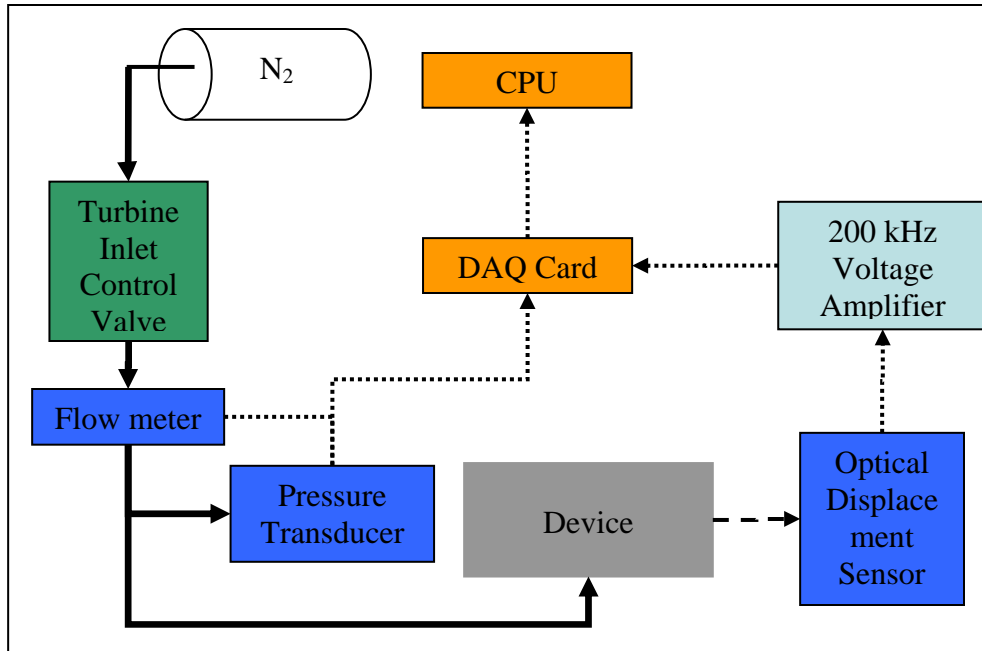


Figure 13. Schematic of the experimental apparatus used for testing the microturbine tribology device.

Note: DAQ = Data Acquisition

5. Results and Discussion

5.1 Experimental Results

Two rotor devices, Device 1 and Device 2, were tested. Device 1 was packaged using Scheme 1 to test the high-speed capability of the bearing. Device 2 was tested using both packaging schemes, with and without a top manifold for pump operation testing. In this report, I only discuss the operation of the turbine. More information on the pump operation can be found in reference 27.

The turbine was characterized using Device 2 with Scheme 1 packaging and after the addition of the pump manifold using Scheme 2 (figure 14). The flow rate required to operate the turbine increases with the addition of the pump manifold due to the air viscous drag. I measured the turbine characterization curve throughout the experiments to track the behavior of the bearing. The curves in figure 14 were taken before the bearing achieved 50,000 revolutions. The turbine was characterized again with Scheme 2 packaging after being operated for more than 2,000,000 revolutions with no degradation observed (figure 15). Bearing operation was continued without significant degradation until 4,500,000 revolutions when testing was stopped and the device dismantled for inspection.

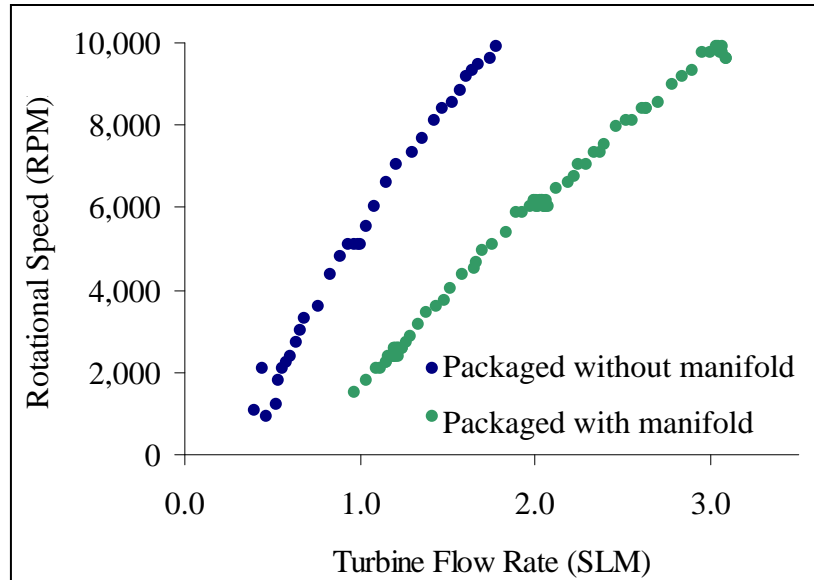


Figure 14. Turbine characterization up to 10,000 rpm in air before and after packaging the pump manifold layer.

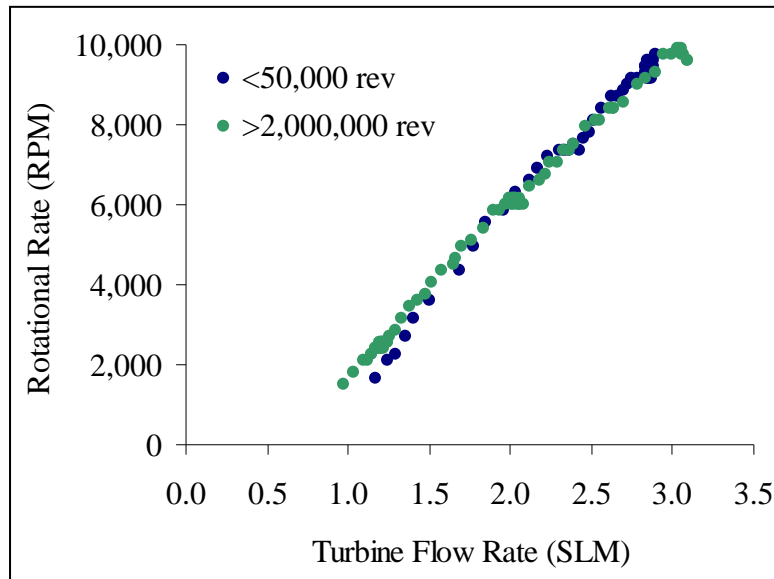


Figure 15. Turbine characterization curve with pump manifold before 50,000 revolutions and after exceeding 2,000,000 revolutions.

A high-speed test was performed using Device 1 with Scheme 1 packaging having the gasket and o-ring to seal the topside of the device. The flow rate through the turbine is limited by the turbine fluidic resistance and the pressure drop from the turbine inlet upstream of the diffuser vanes and the turbine outlet at ambient. I recorded the maximum flow rate with the current experimental apparatus at 13 slm with an estimated turbine pressure drop of 2 psi (assuming half of the pressure drops through the static diffuser vanes and the other half drops through turbine

blades). At this flow rate the radial in-flow air turbine and the modified planar-contact bearing were able to achieve rotational speeds in excess of 85,000 rpm (figure 16), a factor of two greater than previous work (25).

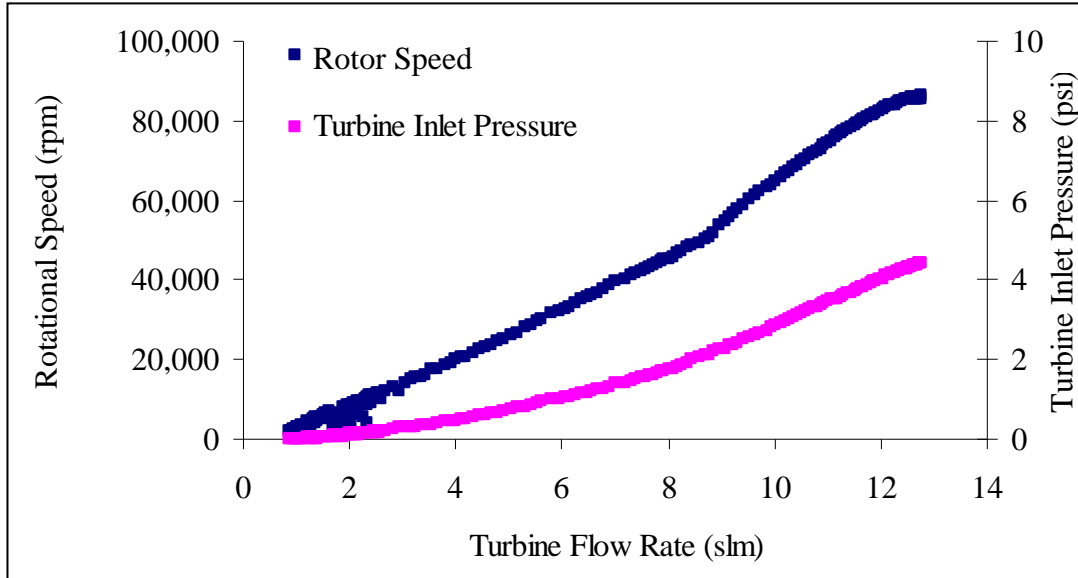


Figure 16. Demonstration of high-speed operation with the planar-contact V.2 bearing and the radial in-flow air turbine.

The speed is expected to increase further with flow rate, but will eventually be limited when the normal force on the rotor becomes too large. Two solutions to increase the flow through the turbine are to increase the turbine blade height and to decrease the fluidic resistance in the inlet line. The coupling between the driving turbine flow and the rotor normal force, however, will eventually limit the speed of the rotor. As the normal force increases so does the power loss to the bearings. It is crucial to decrease the coupling between the turbine rotor speed and the rotor normal force to enable applications that require higher tip speeds.

5.2 Raceway Inspection

A fresh raceway device was first inspected using SEM analysis to observe the thrust surface in proximity to the journal (figure 17). I fabricated this device using the new modified spray coat process and no etch artifact is observed at the edge of the journal when compared to the raceway shown in figure 5, which was fabricated with the nested mask process. A smooth surface minimizes debris generation and allows for longer run times without cleaning.

Device 1 and Device 2 were separated after the experiments to visually inspect the raceway surfaces. The AuSn eutectic layer bonding the two rotor layers together is easily separated using a razor blade inserted at the bond interface. This adhesion layer enabled separation of the device without damaging the surfaces.

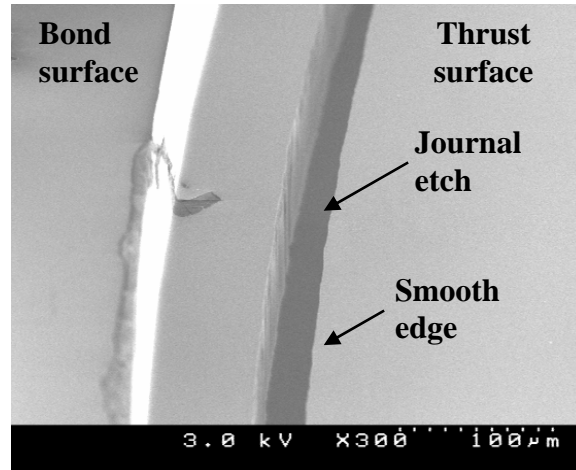


Figure 17. SEM image showing the top down view of the bearing thrust surface using the modified spray coat process.

The raceway surfaces of Device 1 and Device 2 are shown in figure 18. In Device 1 (figure 18a), the wear track depth on both surfaces was estimated to be $1\text{ }\mu\text{m}$ deep with $<100,000$ revolutions with a peak thrust load of 2 N . In Device 2 (figure 18b), the wear track depth on the thrust surface was estimated to be $6.5\text{ }\mu\text{m}$ and on the radial surface was estimated to be $2.5\text{ }\mu\text{m}$ (figure 19) after $4,500,000$ revolutions with an average thrust load below 500 mN . The difference between the wear of Device 1 and Device 2 suggests the rotor wear can change the sag within the rotor (rotor play in the axial direction) over time; however, the performance of the bearing mechanism does not change. Hard coatings with appropriate elastic and hardness properties compared to the stainless steel microballs (e.g., cubic boron nitride or titanium nitride) will be crucial to reduce the wear on the thrust surface for applications where the rotor sag plays an important role in determining the performance. Future work will focus on developing raceways with hard coatings.

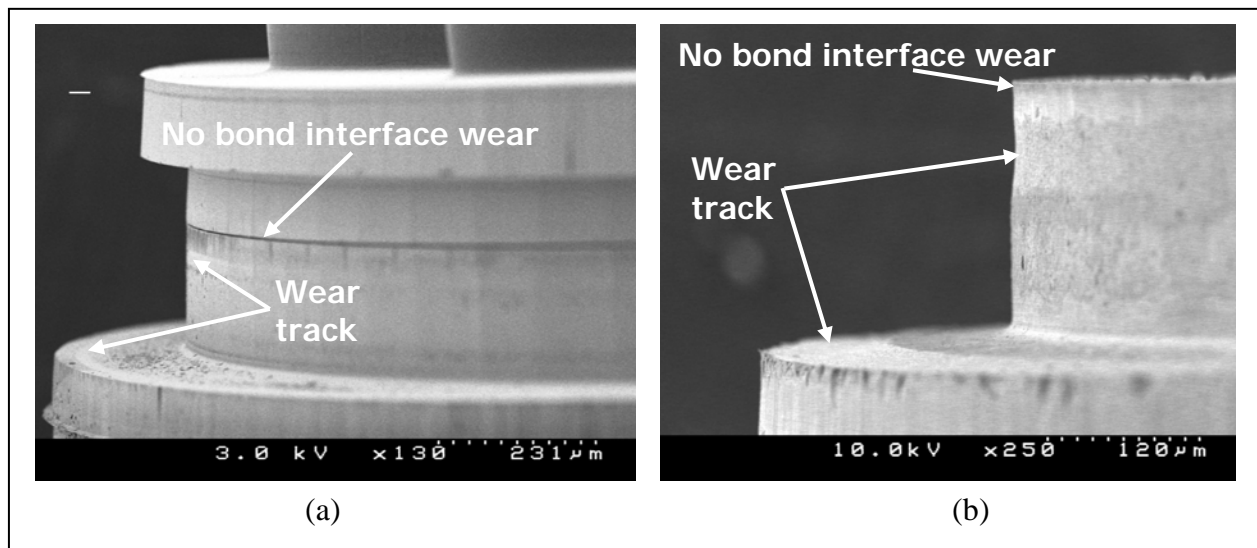


Figure 18. SEM images of the rotor raceway thrust and radial surface for (a) Device 1 and (b) Device 2.

The low wear of Device 1, after reaching speeds greater than 85,000 rpm, suggests that higher-speeds are possible. The failure of this device was caused by fracturing of the raceway due to the enormous thrust force of 2 N, not by the high-speed operation. In this work, the thrust force on the rotor is coupled with the pressure driving the air turbine. The pressure buildup on the topside of the rotor to maintain proper microball contact is not controlled. Methods to bleed the pressure at high speeds can be integrated into the device to help alleviate the pressure buildup while ensuring proper microball contact. Thrust force control or the use of an alternate driving mechanism, like a micromotor, will enable devices to reach higher speeds.

Previously, the radial surface wear track depth was $>15\text{ }\mu\text{m}$ for a device operated for $<100,000$ revolutions (figure 3) versus $2\text{ }\mu\text{m}$ for the device operated for more than 4,500,000 revolutions (figure 19). This is a dramatic improvement that allows for a tighter raceway tolerance to be built-in, reducing the amount of play the rotor has in the radial direction. Rotor play can lead to significant whirl and axial misalignment, which is critical for micromotor and micropump applications. Small changes in the alignment between the stator and rotor can drastically decrease the performance of such machines. The radial surface exhibits less wear than the thrust surface due to low radial loads in the application of micropumps, micromotors, and microgenerators. The low wear of this surface suggests silicon will be suitable for many applications. Like the thrust surface, hard coatings will be required on the radial surface for applications having a need for tighter tolerances. In this case, a growth process will have to be developed to ensure deposition on the sidewall as opposed to the thrust surface where a deposition technique or a growth process will be suitable. Requirements of radial surface coatings will, therefore, limit the materials available.

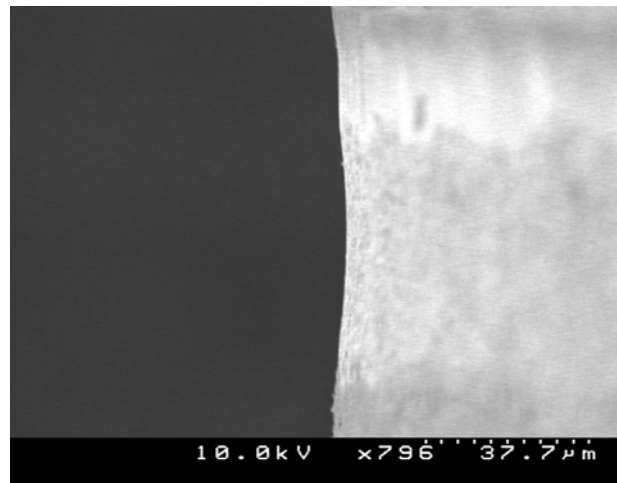


Figure 19. SEM image showing a close-up of the radial raceway surfaces for the new design with the bond interface moved away from the ball wear track.

6. Conclusions

I designed and fabricated a modified bearing raceway to eliminate microfabrication artifacts and minimize raceway wear and debris generation. The modified design positions the bond interface out of the expected microball wear track to reduce the radial raceway surface wear. This positioning eliminates the large debris generation within the raceway and allows for tighter tolerances to be manufactured in the raceway. I also developed a fabrication method, including a spray coat photoresist step, to eliminate surface roughness on the raceway thrust surface and ensure a smooth contact area for the microballs.

The newly developed devices achieved a tremendous improvement in wear over much larger speeds, durations, and rotor forces. I demonstrated over 4,500,000 revolutions without noticeable change in device performance, which is a four-fold improvement from previous work and did not require initial run-in procedures that include multiple cleaning steps. I also demonstrated high-speed operation exceeding 85,000 rpm. The high pressure and flow required to reach the high-speeds using the air turbine caused a significant amount of normal force on the rotor, eventually causing its failure. Low raceway wear suggests that higher speeds are possible for the microball bearing, but redesign of the device to uncouple the normal force on the rotor from the driving turbine is necessary. The work reported here demonstrates the reliability and high-speed capability of microball bearings, which are sufficient for micropump, micromotor applications, and low-speed power generation.

7. References

1. Epstein, A. H. Millimeter-scale, MEMS Gas Turbine Engines. *Proceedings of the ASME Turbo Expo*, Atlanta, GA, June 2003, Paper GT-2003-38866.
2. Isomura, K.; Murayama, M.; Teramoto, S.; Hikichi, K.; Endo, Y.; Togo, S.; Tanaka, S. Experimental Verification of the Feasibility of a 100W Class Micro-scale Gas Turbine at an Impeller Diameter of 10 mm. *J. Micromech. Microeng.* **Sep. 2006**, *16* (9), S254–S261.
3. Peirs, J.; Reynaerts, D.; Verplaetsen, F. A Microturbine for Electric Power Generation. *Sens. Actuators A, Phys.* **June 2004**, *113* (1), 86–93.
4. Fr  chette, L. G.; Lee, C.; Arslan, S.; Liu, Y.-C. Design of a Microfabricated Rankine Cycle Steam Turbine for Power Generation. *Proceedings of the ASME Int. Mech. Eng. Congr. Micro-Electromech. Syst. Division* **2003**, *5*, 335–344.
5. Walther, D. C.; Pisano, A. P. MEMS Rotary Engine Power System: Project Overview and Recent Research Results. *Proceedings of the 4th Int. Symp. MEMS Nanotechnol.* **2003**, 227–234.
6. Zhang, X.; Zheng, D.; Wang, T.; Chen, C.; Cao, J.; Yan, J.; Wang, W.; Liu, J.; Liu, H.; Tian, J.; Li, X.; Yang, H.; Xia, B. A Preliminary Study of a Miniature Planar 6-cell PEMFC Stack Combined with a Small Hydrogen Storage Canister. *J. of Power Sources* **2007**, *166* (2), 441–444.
7. Kamarudin, S. K.; Daud, W.R.W.; Ho, S. L.; Hasran, U. A. Overview on the Challenges and Developments of Micro-direct Methanol Fuel Cells (DMFC). *J. of Power Sources* **2007**, *163* (2), 743–754.
8. Fr  chette, L. G.; Jacobson, S. A.; Breuer, K. S.; Ehrich, F. F.; Ghodssi, R.; Khanna, R.; Wong, C. W.; Zhang, X.; Schmidt, M. A.; Epstein, A. H. High-Speed Microfabricated Silicon Turbomachinery and Fluid Film Bearings. *J. of Microelectromechanical Systems* **2005**, *14*, 141–152.
9. Ruffert, C.; Gehrking, R.; Ponick, B.; Gatzen, H. H. Magnetic Levitation Assisted Guide for a Linear Micro-Actuator. *IEEE Transaction on Magnetics* **2006**, *42*, 3785.
10. Shearwood, C.; Ho, K. Y.; Williams, C. B.; Gong, H. Development of a Levitated Micromotor for Application as a Gyroscope. *Sensors and Actuators A: Physical* **2000**, *83*, 85.
11. Williams, C. B.; Shearwood, C.; Mellor, P. H.; Yates, R. B. Modeling and Testing of a Frictionless Levitated Micromotor. *Sensors and Actuators A: Physical* **1997**, *61*, 469.

12. Jeon, J. U.; Woo, S. J.; Higuchi, T. Variable-capacitance Motors with Electrostatic Suspension. *Sensors and Actuators A: Physical* **1999**, *75*, 289.
13. Wu, X. S.; Chen, W. Y.; Zhao, X. L.; Zhang, W. P. Micromotor with Electromagnetically Levitated Rotor Using Separated Coils. *Electronics Letters* **2004**, *40*, 996–997.
14. Mehregany, M.; Gabriel, K. J.; Trimmer, W.S.N. Integrated Fabrication of Polysilicon Mechanisms. *IEEE Transactions on Electron Devices* **1988**, *35*, 719–723.
15. Deng, K.; Ko, W. H.; Michael, G. M. A Preliminary Study on Friction Measurements in MEMS. *International Conference on Solid-State Sensors and Actuators, TRANSDUCERS '91*, San Francisco, CA, 1991.
16. Noguchi, K.; Fujita, H.; Suzuki, M.; Yoshimura, N. The Measurements of Friction on Micromechatronics Elements. *IEEE Micro Electro Mechanical Systems (MEMS'91)*, Nara, Japan, 1991.
17. Zhang, W.; Meng, G.; Li, H. Electrostatic Micromotor and its Reliability. *Microelectronics Reliability* **2005**, *45*, 1230.
18. Ghodssi, R.; Denton, D.D.; Seireg, A. A.; Howland, B. Rolling Friction in a Linear Microactuator. *J. of Vacuum Science and Technology A* **1993**, *11*, 803–807.
19. Lin, T.-W.; Modafe, A.; Shapiro, B.; Ghodssi, R. Characterization of Dynamic Friction in MEMS-based Microball Bearings. *IEEE Transactions on Instrumentation and Measurement* **2004**, *53* (3), 839–846.
20. Tan, X.; Modafe, A.; Ghodssi, R. Measurement and Modeling of Dynamic Rolling Friction in Linear Microball Bearings. *J. of Dynamic Systems, Measurement, and Control* **2006**, *128*, 891–898.
21. Modafe, A.; Ghalichechian, N.; Lang, J. H.; Ghodssi, R. A Microball-Bearing-Supported Linear Electrostatic Micromotor with Benzocyclobutene Polymer Insulating Layers. *The 13th International Conference on Solid-State Sensors, Actuators, and Microsystems (Transducers '05)*, Seoul, Korea, 2005.
22. Ghalichechian, N.; Modafe, A.; Beyaz, M.; Ghodssi, R. Design, Fabrication, and Characterization of a Rotary Micromotor Supported on Microball Bearings. *J. of Microelectromechanical Systems (JMEMS)* **2007**, vol. In Press.
23. Waits, C. M.; Geil, B.; Ghodssi, R. Encapsulated Ball Bearings for Rotary Micro Machines. *J. of Micromechanics and Microengineering* **2007**, *17*, S224–S229.

24. Waits, C. M.; Jankowski, N.; Geil, B.; Ghodssi, R. MEMS Rotary Actuator Using an Integrated Ball Bearing and Air Turbine. *Proceedings of the 14th International Conference on Solid-State Sensors, and Microsystems (Transducers '07)*. Lyon, France, 10–14 June 2007.
25. McCarthy, M.; Waits, C. M.; Ghodssi, R. Dynamic Friction and Wear in a Planar-Contact Encapsulated Microball Bearing using an Integrated Microturbine. Accepted for publication in *J. of Microelectromechanical Systems*, Nov 2008.
26. Harris, Tedric A. *Rolling Bearing Analysis*, 3rd ed.; John Wiley & Sons, Inc.: New York, 1991.
27. Waits, C. M. Microturbopump Utilizing Microball Bearings. PhD. Thesis, University of Maryland, College Park, MD, 2008.

List of Symbols, Abbreviations, and Acronyms

Au	gold
AuSn	gold-tin
Cr	chromium
DAQ	Data Acquisition
DRIE	deep reactive ion etching
FFT	Fast Fourier Transform
MEMS	micro-electromechanical systems
SEM	scanning electron microscope

No. of Copies	Organization	No. of Copies	Organization
1 ELEC	ADMNSTR DEFNS TECHL INFO CTR ATTN DTIC OCP 8725 JOHN J KINGMAN RD STE 0944 FT BELVOIR VA 22060-6218	1	US ARMY RSRCH LAB ATTN AMSRD ARL CI OK TP TECHL LIB T LANDFRIED BLDG 4600 ABERDEEN PROVING GROUND MD 21005-5066
1	DARPA ATTN IXO S WELBY 3701 N FAIRFAX DR ARLINGTON VA 22203-1714	1	DIRECTOR US ARMY RSRCH LAB ATTN AMSRD ARL RO EV W D BACH PO BOX 12211 RESEARCH TRIANGLE PARK NC 27709
1 CD	OFC OF THE SECY OF DEFNS ATTN ODDRE (R&AT) THE PENTAGON WASHINGTON DC 20301-3080		
1	US ARMY RSRCH DEV AND ENGRG CMND ARMAMENT RSRCH DEV AND ENGRG CTR ARMAMENT ENGRG AND TECHNLGY CTR ATTN AMSRD AAR AEF T J MATTS BLDG 305 ABERDEEN PROVING GROUND MD 21005-5001	12	US ARMY RSRCH LAB ATTN AMSRD ARL CI OK PE TECHL PUB ATTN AMSRD ARL CI OK TL TECHL LIB ATTN AMSRD ARL SE D E SHAFFER ATTN AMSRD ARL SE DP B GEIL ATTN AMSRD ARL SE DP B HANRAHAN ATTN AMSRD ARL SE DP B MORGAN ATTN AMSRD ARL SE DP C M WAITS ATTN AMSRD ARL SE DP D SHARAR ATTN AMSRD ARL SE DP I LEE ATTN AMSRD ARL SE DP J HOPKINS ATTN AMSRD ARL SE DP N JANKOWSKI ATTN IMNE ALC HRR MAIL & RECORDS MGMT ADELPHI MD 20783-1197
1	PM TIMS, PROFILER (MMS-P) AN/TMQ-52 ATTN B GRIFFIES BUILDING 563 FT MONMOUTH NJ 07703		
1	US ARMY INFO SYS ENGRG CMND ATTN AMSEL IE TD F JENIA FT HUACHUCA AZ 85613-5300		
1	COMMANDER US ARMY RDECOM ATTN AMSRD AMR W C MCCORKLE 5400 FOWLER RD REDSTONE ARSENAL AL 35898-5000		
1	US GOVERNMENT PRINT OFF DEPOSITORY RECEIVING SECTION ATTN MAIL STOP IDAD J TATE 732 NORTH CAPITOL ST NW WASHINGTON DC 20402		
		TOTAL: 22 (1 PDF, 1 CD, 20 HCS)	

INTENTIONALLY LEFT BLANK.